Cooperated Spectral Low-Rankness Prior and Deep Spatial Prior for HSI Unsupervised Denoising

Qiang Zhang, Qiangqiang Yuan, *Member, IEEE*, Meiping Song, *Member, IEEE*, Haoyang Yu, *Member, IEEE*, and Liangpei Zhang, *Fellow, IEEE*

***Abstract*— Model-driven methods and data-driven methods have been widely developed for hyperspectral image (HSI) denoising. However, there are pros and cons in both model-driven and data-driven methods. To address this issue, we develop a self-supervised HSI denoising method via integrating model-driven with data-driven strategy. The proposed framework simultaneously cooperates the spectral low-rankness prior and deep spatial prior (SLRP-DSP) for HSI self-supervised denoising. SLRP-DSP introduces the Tucker factorization via orthogonal basis and reduced factor, to capture the global spectral low-rankness prior in HSI. Besides, SLRP-DSP adopts a self-supervised way to learn the deep spatial prior. The proposed method doesn't need a large number of clean HSIs as the label samples. Through the self-supervised learning, SLRP-DSP can adaptively adjust the deep spatial prior from self-spatial information for reduced spatial factor denoising. An alternating iterative optimization framework is developed to exploit the internal low-rankness prior of third-order tensors and the spatial feature extraction capacity of convolutional neural network. Compared with both existing model-driven methods and data-driven methods, experimental results manifest that the proposed SLRP-DSP outperforms on mixed noise removal in different noisy HSIs.**

***Index Terms*— Hyperspectral, denoising, self-supervised, spectral low-rankness prior, deep spatial prior, alternating iterative optimization.**

I. Introduction

HYPERSPECTRAL image (HSI) simultaneously captures the spatial and spectral information of the observed objects [1]. Through the wide and dense spectral feature, HSI can better distinguish the physical differences between various surface materials, compared with natural image[2]. Therefore, HSI has been widely put into practice such as classification, object detection, anomaly detection and the like [3].

Manuscript received 5 January 2022; revised 13 July 2022 and 4 September 2022; accepted 6 September 2022. Date of publication 10 October 2022; date of current version 14 October 2022. This work was supported in part by the National Natural Science Foundation of China under Grant 41922008, Grant 42101350, Grant 61971082, and Grant 61971319. The associate editor coordinating the review of this manuscript and approving it for publication was Prof. Lisimachos Paul Kondi. *(Corresponding authors: Qiangqiang Yuan; Meiping Song.)*

Qiang Zhang, Meiping Song, and Haoyang Yu are with the Center of Hyperspectral Imaging in Remote Sensing (CHIRS), Information Science and Technology College, Dalian Maritime University, Dalian 116026, China (e-mail: whuqzhang@gmail.com; smping@163.com; yuhy@dlmu.edu.cn).

Qiangqiang Yuan is with the School of Geodesy and Geomatics, Wuhan University, Wuhan 430079, China (e-mail: yqiang86@gmail.com).

Liangpei Zhang is with the State Key Laboratory of Information Engineering in Surveying, Mapping and Remote Sensing, Wuhan University, Wuhan 430079, China (e-mail: zlp62@whu.edu.cn).

Digital Object Identifier 10.1109/TIP.2022.3211471

However, everything has two sides including HSI. Due to the atmospheric interference, sensor tremor and signal response, almost all of the acquired HSIs are inevitably polluted by various noise to different degrees [4]. The noise types include Gaussian noise, Poisson noise, pepper noise, stripe noise, and mixed noise. What's worse, the noise level and type usually vary in different bands of noisy HSIs [5].

To address this noise pollution issue in HSI, plenty of HSI denoising works have been presented during last twenty years [6], [7], [8]. Different from natural image denoising, HSI denoising task needs to simultaneously consider the spectral feature preservation and remove the mixed noise [9]. What's more, the complementary and redundant spectral information can be effectively utilized for enhancing the HSI denoising results [10]. Therefore, spectral-spatial based methods for HSI denoising have gradually become the mainstream strategy [11], [12]. From the perspective of thoughts, most HSI denoising methods could be generally split into two categories: 1) Model-driven HSI denoising methods, and 2) data-driven HSI denoising methods. Specific literatures and evaluations of the two type methods are given as follows.

1) Model-driven HSI denoising methods: Model-driven methods mainly utilize the intrinsic characteristics of HSI and variational framework, to remove the mixed noise in HSI. Up to now, total variation (TV) [13], [14], [15], non-local prior [16], sparse representation [17], [18], [19], and low-rank matrix or tensor factorization [20], [21], [22], [23], [24], [25] have been applied for this field. For example, Maggioni *et al.* [16] stacked the non-local cubes in 4D transform groups for processing volumetric data. Peng *et al.* [26] simultaneously considered the spatial non-local similarity and the spectral consistency, to remove the additive noise in HSI. Zhang *et al.* [20] transformed the HSI recovery task into the low-rank matrix factorization, through unfolding the 3D spatio-spectral cube into the 2D matrix. Further, He *et al.* [21] integrated the TV term with low-rank matrix representation, and performed well on spatial details preserving for HSI denoising. Zhuang and Bioucas [19] united the low-rank subspaces in HSI with self-similarity traits, which can fast remove mixed noise and inpaint deadlines in corrupted HSI. Zhao *et al.* [17] utilized the spectral-spatial redundancy and relevant in HSI, via combining low-rank matrix and sparse representation for HSI noise reduction.

In addition to the above methods, low-rank tensor decomposition [27] has been mostly utilized for HSI denoising in recent

years. Xie *et al.* [22] developed a tensor sparsity estimation in multispectral image denoising, to constraint the internal low-rank prior. Fan *et al.* [28] integrated the both spatial and spectral TV regularization terms into the low-rank tensor decomposition model for HSI denoising. Xiong *et al.* [29] bring the L_0 gradient regularization into the local spatio-spectral low-rank tensor framework, which could simultaneously suppress spectral distortion and preserve spatial details of HSI. Chen *et al.* [18] combined the weighted group sparsity regularization with low-rank tensor decomposition for HSI denoising. Zheng *et al.* [30] built a fibered low-rank tensor minimizing model through ADMM optimization strategy, to flexibly depict the structure of noisy HSI.

2) Data-driven HSI denoising methods: Differing with model-driven methods, data-driven methods adaptively adjust the trainable parameters from external data and label, via deep learning framework [31], [32], [33]. Though iteratively optimizing the deep neural network from large labeled data, deep learning could effectively extract internal features in assigned tasks. With the quick development of deep learning such as convolutional neural network (CNN), it has been rapidly utilized for natural image denoising [34] and super-resolution [35]. Apart from nature image, deep learning is also gradually employed in remote sensing image recovery [36], [37], [38] and super-resolution [39], [40], [41], which fully exploit the imaging model to improve the learning ability of CNN. For HSI denoising, several deep learning-based literatures have also been proposed in recent years [42], [43], [44], [45], [46], [47], [48], [49], [50].

For instance, Xie *et al.* [42] combined multi-layer CNN with learnable non-linear functions to suppress noise in HSI. Yuan *et al.* [43] introduced the multi-scale and multi-level units into the spatio-spectral CNN model, to learn the non-linear map from noisy HSI to clean HSI. Further, Zhang *et al.* [44] utilized both spatial and spectral gradient as the input terms of deep CNN, which outperformed on mixed noise removal in HSI. Chang *et al.* [45] exploit multi-channel 2D CNN filters named HSI-DeNet for HSI denoising. Via splitting 3D CNN filters into spatial filters and spectral filters, Dong *et al.* [46] relied on the original 3D U-Net and generated training samples through RGB images for HSI noise reduction. Wei *et al.* [47] developed a quasi-recurrent 3D CNN framework, which could effectively remove polluted noise in HSI under multiple complicated environments. Beyond pure data-driven strategy, Zhang *et al.* [48] simultaneously modeled the noise distribution and reduced mixed noise in HSI through a deep Bayesian posterior structure. It achieved reliable results for HSI denoising especially for non-i.i.d noise.

In summary, there are pros and cons, in both model-driven and data-driven methods for HSI denoising [51]. Model-driven methods can accurately depict the inherent prior of HSI, through introducing low-rank, TV, and non-local prior. However, these model-driven HSI denoising methods have weakness on manually crucial parameters, such as rank threshold and iteration count [52]. What's worse, most model-driven methods usually take long consuming-time, because of the complex iterating optimization.

In terms of the data-driven HSI denoising methods, these methods usually perform more efficiently than model-driven methods, without carefully adjusting model parameters [53]. Nevertheless, deep learning-based HSI denoising framework still needs a large number of clean HSIs as the label samples. However, the clean HSIs are actually rare and hardly obtained in most imaging environment [54]. Except for this limitation, the simulated noise distribution for clean HSI samples is usually hard to agree with the actual noise distribution in acquired noisy HSIs, because of the complicated imaging mechanism [55]. This issue greatly affects the generality of deep networks especially for HSI blind noise reduction.

From above-mentioned perspectives, can we jointly combine the merits of model-driven with data-driven methods, and overcome the disadvantages of the two type methods? Aiming at this motivation, we develop a novel self-supervised method for HSI denoising through integrating model-driven with data-driven strategy. The main contributions of this work are described as follows:

1) The proposed framework simultaneously cooperates the spectral low-rankness prior and deep spatial prior (SLRP-DSP) for HSI self-supervised denoising.
2) Through alternating iterative optimization, SLRP-DSP can both exploit the internal low-rank prior of HSI and spatial feature extraction capacity of CNN.
3) Different from supervised denoising methods, SLRP-DSP adopts a self-supervised way to denoise the deep spatial prior. The proposed SLRP-DSP needn't a large number of clean HSIs as label samples.
4) Compared with both existing model-driven and data-driven HSI denoising methods, experimental results manifest that the proposed SLRP-DSP outperforms on mixed noise removal in different noisy HSIs.

The rest of this work is scheduled below. Section II provides the problem formulation and describes the details of SLRP-DSP. Section III shows the HSI denoising results of the simulated and real experiments. Then a discussion is given in Section IV. Finally, the conclusion and prospect are summarized in Section V.

II. Proposed HSI Restoration Model

A. Notations and Definitions

Before describing the proposed method, we firstly give the related notations and definitions in this work for better understanding.

To distinguish data dimension, the scalar, vector, matrix and tensor values in this work are respectively represented as x (lowercase and italic), $\mathbf{x}$ (lowercase and bold), $\mathbf{X}$ (uppercase and bold) and $\mathcal{X}$ (uppercase and Euclid math font) formats. In terms of a third-order tensor $\mathcal{X}$ value, $\mathcal{X}(:, k_2, k_3)$, $\mathcal{X}(k_1, :, k_3)$ and $\mathcal{X}(k_1, k_2, :)$ stand for the tube of tensor $\mathcal{X}$ in three dimensions [56]. Besides, $\mathbf{X}_{(i)}$ is denoted as the unfolding matrix format of the third-order tensor $\mathcal{X}$, with the size of $k_i \times \prod_{n \neq i} k_n$ [57].

Definition 1 (Tensor-Matrix Product): In terms of a third-order tensor $\mathcal{X} \in \mathbb{R}^{k_1 \times k_2 \times k_3}$ and matrix $\mathbf{A} \in \mathbb{R}^{k_3 \times k_4}$,

the mode-i tensor-matrix product [58] is formatted as:

$$\mathcal{Y} = \mathcal{X} \times_i \mathbf{A} \Leftrightarrow \mathbf{Y}_{(i)} = \mathbf{A}\mathbf{X}_{(i)}$$

Definition 2 (Tensor Tucker Rank): In terms of a third-order tensor $\mathcal{X} \in \mathbb{R}^{k_1 \times k_2 \times k_3}$, its Tucker rank [59] is denoted as:

$$Rank_T(\mathcal{X}) = (Rank(\mathbf{X}_{(1)}), Rank(\mathbf{X}_{(2)}), Rank(\mathbf{X}_{(3)}))$$

B. Problem Formulation

The HSI degraded procedure can be simply formulated as the following equation:

$$\mathcal{Y} = \mathcal{X} + \mathcal{N} \tag{1}$$

where the noisy HSI $\mathcal{Y} \in \mathbb{R}^{k_1 \times k_2 \times k_3}$ could be treated as a third-order tensor, with the spatial size $k_1 \times k_2$ and spectral number k_3. $\mathcal{X} \in \mathbb{R}^{k_1 \times k_2 \times k_3}$ represents the clean HSI. $\mathcal{N} \in \mathbb{R}^{k_1 \times k_2 \times k_3}$ stands for the additive noise such as Gaussian noise, Poisson noise, pepper noise, stripe noise, and mixed noise in HSI.

The crucial issue for HSI denoising task is to estimate noise-free HSI $\mathcal{X}$ from noisy HSI $\mathcal{Y}$. Apparently, this is an inverse problem where the known variables are less than the unknown variables. Therefore, we need to impose suitable priors to address this issue. Generally, a typical framework for HSI denoising could be simplified as [60]:

$$\arg\min_{\mathcal{X}} \frac{1}{2} \|\mathcal{Y} - \mathcal{X}\|_F^2 + \mu \cdot \mathcal{T}(\mathcal{X}) \tag{2}$$

where $\mathcal{T}(\mathcal{X})$ stands for the regularization term to utilize internal HSI prior. μ is the balanced parameter of the regularization term. In consideration that HSI is regarded as a natural third-order tensor, we can exploit the low-rankness prior of HSI. Mathematically, a clean HSI $\mathcal{X} \in \mathbb{R}^{k_1 \times k_2 \times k_3}$ can be approximatively factorized as two parts: a spectral orthogonal basis matrix $\mathbf{A} \in \mathbb{R}^{k_3 \times r}$ ($r \ll k_3$) to capture the common subspace in different bands, and a spatial reduced factor $\mathcal{B} \in \mathbb{R}^{k_1 \times k_2 \times r}$. The global spectral low-rankness prior in clean HSI $\mathcal{X}$ can be represented through Tucker factorization:

$$\mathcal{X} = \mathcal{B} \times_3 \mathbf{A} \tag{3}$$

where the spectral orthogonal basis matrix $\mathbf{A}$ captures the communal subspace in spectral dimension. And the spatial reduced factor $\mathcal{B}$ reflects spatial feature in HSI. Though imposing the low-rank tensor factorization strategy, the generalized HSI denoising framework in (2) could be transformed as:

$$\begin{aligned} &\arg\min_{\mathbf{A},\mathcal{B}} \frac{1}{2} \|\mathcal{Y} - \mathcal{B} \times_3 \mathbf{A}\|_F^2 + \mu \cdot \mathcal{T}(\mathcal{B}) \\ &\text{s.t. } \mathbf{A}^\top \mathbf{A} = \mathbf{I} \end{aligned} \tag{4}$$

where the orthogonal constraint for $\mathbf{A}$ boosts the representation held in spectral factor $\mathbf{A}$ to be more distinct [61].

C. Proposed SLRP-DSP Model

Based on the Tucker factorization strategy in (4), we simultaneously cooperate the spectral low-rankness prior and deep spatial prior (SLRP-DSP) for HSI self-supervised denoising below:

$$\begin{aligned} \mathbf{A}, \mathcal{B}, \mathcal{Z} = \arg\min_{\mathbf{A},\mathcal{B},\mathcal{Z}} &\frac{1}{2} \|\mathcal{Y} - \mathcal{Z}\|_F^2 + \frac{\alpha\beta}{2} \|\mathcal{Z} - \mathcal{B} \times_3 \mathbf{A}\|_F^2 \\ &+ \alpha \cdot \mathcal{R}_{SLRP}(\mathcal{Z}, \mathbf{A}) + \beta \cdot \mathcal{T}_{DSP}(\mathcal{Z}, \mathcal{B}) \end{aligned} \tag{5}$$

where $\mathcal{R}_{SLRP}(\mathcal{Z}, \mathbf{A})$ and $\mathcal{T}_{DSP}(\mathcal{Z}, \mathcal{B})$ refer to the spectral low-rankness prior and deep spatial prior, respectively. α and β represent the balanced parameters of the two regularizations. $\mathcal{Z}$ is the latent clean HSI for noisy HSI $\mathcal{Y}$:

$$\mathcal{Z}^{i+1} = \arg\min_{\mathcal{Z}} \frac{1}{2} \|\mathcal{Y} - \mathcal{Z}\|_F^2 + \frac{\alpha\beta}{2} \left\| \mathcal{Z} - \mathcal{Z}^i \right\|_F^2 \tag{6}$$

The flowchart of the proposed SLRP-DSP for HSI self-supervised denoising is depicted in Fig. 1. The integral model can be separated into three parts: 1) Spectral low-rankness prior; 2) Deep spatial prior; 3) Alternating iterative optimization. Descriptions of these parts are given below.

1) Spectral Low-Rankness Prior: As shown in Fig. 1, we impose low-rank tensor factorization framework to estimate the spectral orthogonal basis matrix $\mathbf{A}$ by updating:

$$\mathbf{A}^{i+1} = \arg\min_{\mathbf{A}} \mathcal{R}_{SLRP}(\mathcal{Z}^i, \mathbf{A}) + \frac{\alpha}{2} \left\| \mathbf{A} - \mathbf{A}^i \right\|_F^2 \tag{7}$$

where α denotes as the proximal parameter. $\mathbf{A}^i$ stands for the i-th iteration value. To approximately solve this equation, we employ Tucker rank to exploit spectral low-rankness:

$$\mathcal{R}_{SLRP}(\mathcal{Z}^i, \mathbf{A}) = \text{SVD}_r(\mathbf{Z}^i{}_{(3)}) \quad s.t.\ \mathbf{A}^{i\top} \mathbf{A}^i = \mathbf{I} \tag{8}$$

where $\text{SVD}_r(\cdot)$ denotes the interception result with Tucker rank parameter r under matrix singular value decomposition (SVD) economy mode. It should be highlighted that this Tucker rank value r is far less than the band number k_3 of the latent HSI $\mathcal{Z} \in \mathbb{R}^{k_1 \times k_2 \times k_3}$ ($r \ll k_3$).

For the spatial reduced factor $\mathcal{B}$ in Fig. 1, we estimate it through updating the following solution:

$$\mathcal{B}^{i+1} = \arg\min_{\mathcal{B}} \mathcal{T}_{DSP}(\mathcal{Z}^i, \mathcal{B}) + \frac{\beta}{2} \left\| \mathcal{B} - \hat{\mathcal{B}}^i \right\|_F^2 \tag{9}$$

After estimating the spectral orthogonal basis matrix $\mathbf{A}$, the noisy spatial reduced factor $\hat{\mathcal{B}}$ can be calculated by:

$$\hat{\mathcal{B}}^i = \mathcal{Z}^i \times_3 \mathbf{A}^{i\top} \tag{10}$$

where mode-3 tensor-matrix product is employed between the latent HSI $\mathcal{Z}^i$ and transposed spectral orthogonal basis matrix $\mathbf{A}^i$. Then (9) is transformed as:

$$\mathcal{B}^{i+1} = \arg\min_{\mathcal{B}} \mathcal{T}_{DSP}(\mathcal{Z}^i, \mathcal{B}, \hat{\mathcal{B}}^i) + \frac{\beta}{2} \left\| \mathcal{B} - \hat{\mathcal{B}}^i \right\|_F^2 \tag{11}$$

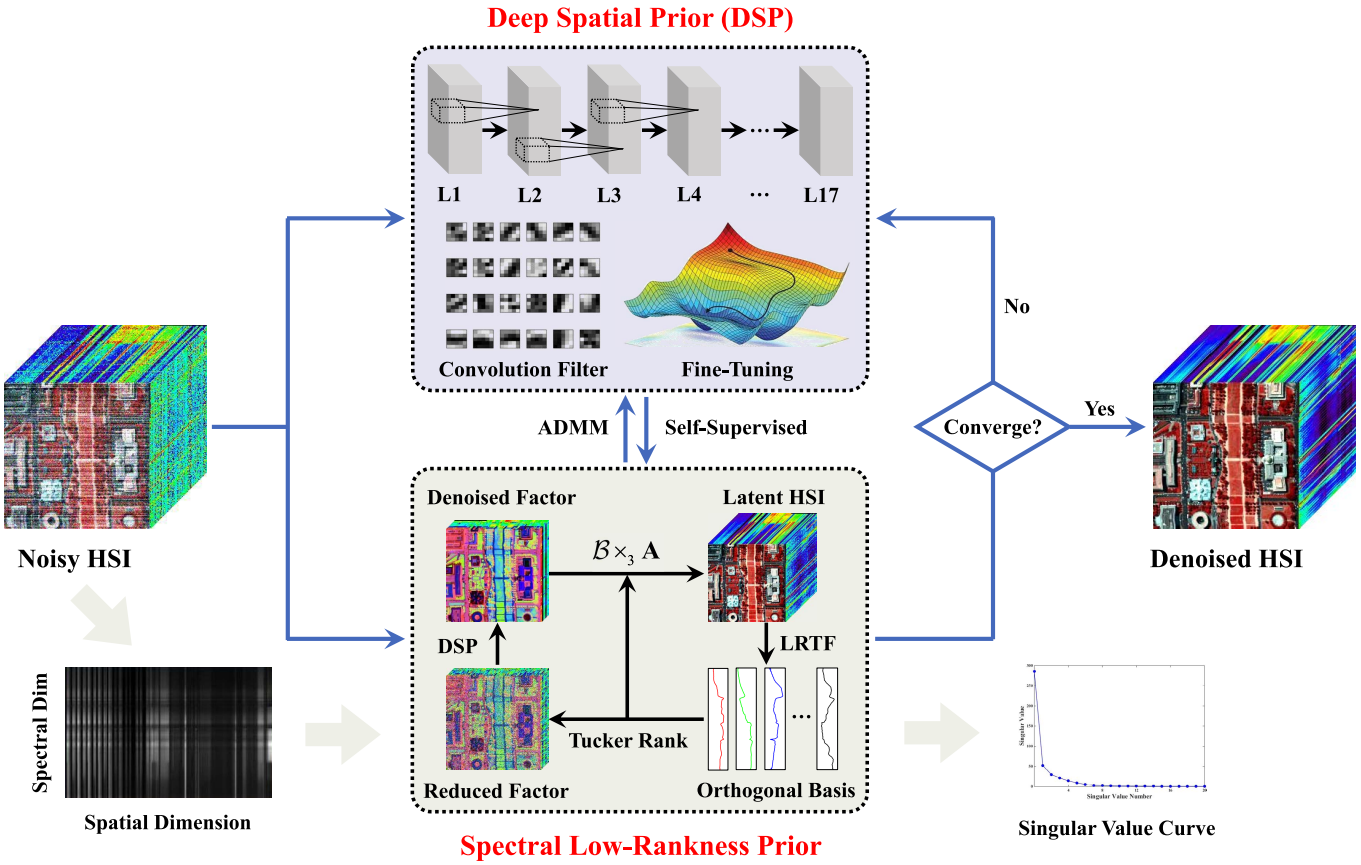

Fig. 1. Flowchart of the proposed SLRP-DSP for HSI self-supervised denoising.

2) Deep Spatial Prior: As described in Fig. 1, the acquired spatial reduced factor $\hat{\mathcal{B}}^i \in \mathbb{R}^{k_1 \times k_2 \times r}$ is usually noisy though global spectral low-rankness prior and LRTF strategy. Therefore, we lead in a deep spatial prior to adaptively remove polluted noise in spatial reduced factor $\hat{\mathcal{B}}^i$:

$$\mathcal{B}^i = \underset{j=1}{\overset{r}{\Im}} \left\langle \mathcal{T}_{DSP}(\hat{\mathcal{B}}^i(:,:,j)) \right\rangle \tag{12}$$

where $\mathcal{T}_{DSP}(\cdot)$ denotes the deep spatial denoiser for each band of $\hat{\mathcal{B}}^i$. We initialize the trainable network parameters of this deep denoiser via DnCNN [34] model (blind, 17 CNN layers). The convolutional filters in $\mathcal{T}_{DSP}$ are visualized in Fig. 1. Detailed fine-tuning operation of the deep spatial denoiser $\mathcal{T}_{DSP}$ is described in the following alternating iterative optimization. $\Im\langle\cdot\rangle$ stands for the band-by-band mode for $\hat{\mathcal{B}}^i$. It is carried out through the band sequential traversal way. Then the updated latent clean HSI $\mathcal{Z}^{i+1}$ is estimated as:

$$\mathcal{Z}^{i+1} = \mathcal{B}^i \times_3 \mathbf{A}^i \tag{13}$$

3) Alternating Iterative Optimization: According to (5), (6), (7) and (11), the spectral low-rankness prior and deep spatial prior are iteratively updated through alternating iterative optimization. The proposed framework uses both alternating direction method of multipliers (ADMM) and back-propagation, as shown in Fig. 1. For the deep spatial denoiser $\mathcal{T}_{DSP}$, we utilize the self-supervised strategy to adjust the parameters. The self-supervised loss function ζ_{DSP} is defined as:

$$\zeta_{DSP} = \frac{1}{2N} \sum_{n=1}^{N} \left\| (\mathcal{Y}_p - \mathcal{Z}_p^i)_n - \mathcal{T}_{DSP}(\mathcal{Y}_p)_n \right\|_2^2 \tag{14}$$

where N stands for the total number of fine-tuning patch samples. $\mathcal{Z}_p^i$ denotes the patch samples of the latent HSI $\mathcal{Z}^i$, for the p-th epoch fine-tuning operation:

$$\mathcal{Z}_p^i = \underset{j=1}{\overset{k_3}{\Im}} \left\langle Patch(\mathcal{Z}^i(:,:,j)) \right\rangle \tag{15}$$

where function $Patch(\cdot)$ represents that we crop the holistic band image as the small patches in the fine-tuning procedure, through global spatial traversal operation. Then these patches are selected as training samples for the deep spatial denoiser. Then BP and gradient descent are employed for optimizing the trainable parameters $\mathbf{W}_p$ and b_p in each layer:

$$\zeta_{DSP}\left\{\mathbf{W}_{p+1}, b_{p+1}\right\} = \zeta\left\{\mathbf{W}_p, b_p\right\} + \sigma \cdot \frac{\partial \zeta}{\partial\left\{\mathbf{W}_p, b_p\right\}} \tag{16}$$

where the self-supervised training keeps the chain rule for updating $\mathbf{W}_p$ and b_p. σ is the learning rate in the fine-tuning procedure. In the next $(p+1)$-th fine-tuning epoch, all the patch samples need to be randomly reordered and resorted, for enhancing the generalization of the deep spatial denoiser:

$$\mathcal{Z}_{p+1}^i = Sort \underset{j=1}{\overset{k_3}{\Im}} \left\langle \mathcal{Z}_p^i(:,:,j) \right\rangle \tag{17}$$

Then the convergence condition of the self-supervised spatial denoiser $\mathcal{T}_{DSP}$ is checked by:

$$\left\|\mathcal{T}_{DSP}(\mathcal{B}^i)-\mathcal{B}^i\right\|_F / \left\|\mathcal{B}^i\right\|_F < \varepsilon \tag{18}$$

where ε stands for the tiny threshold (fixed as 1e-4). If current epoch meets this condition, we stop the fine-tuning operation in optimizing self-supervised spatial denoiser $\mathcal{T}_{DSP}$. Otherwise, we continue this fine-tuning operation until meeting the convergence condition or arriving the maximum epoch. Through the self-supervised learning strategy, the proposed SLRP-DSP method can adaptively remove blind noise in the spatial reduced factor $\hat{\mathcal{B}}^i$ via the deep spatial denoiser $\mathcal{T}_{DSP}$.

To address the integral optimization in (5), we utilize ADMM in the proposed SLRP-DSP. The Lagrange auxiliary multiplier $\mathcal{Q}^i$ is introduce into the iterative framework. Then, the latent HSI $\mathcal{Z}^i$ in (6) could be formulated as:

$$\mathcal{Z}^{i+1}=\arg\min_{\mathcal{Z}^i}\frac{1}{2}\left\|\mathcal{Y}-\mathcal{Z}^i\right\|_F^2+\frac{1}{2}\left\|\mathcal{Z}^i-\mathcal{B}^i\times_3\mathbf{A}^i\right\|_F^2 + f(\mathcal{B}^i,\mathbf{A}^i,\mathcal{Z}^i,\mathcal{P}^i) \tag{19}$$

To solve (19), we can alternately update:

$$\mathcal{P}^{i+1}=\mathcal{P}^i+\beta^i\cdot(\mathcal{B}^i\times_3\mathbf{A}^i-\mathcal{Z}^i) \tag{20}$$

$$\mathcal{Z}^{i+1}=\mathcal{Z}^i-1/\beta^i\cdot\mathcal{P}^{i+1} \tag{21}$$

$$\beta^{i+1}=\kappa\cdot\beta^i \tag{22}$$

where κ is a decay factor for penalty parameter β^i. During the alternating iterative optimization, the quality of the latent HSI $\mathcal{Z}^i$ is gradually improved via spectral denoising in (8) and spatial denoising (12). Therefore, the Tucker rank value r is substantially increased in the proposed framework:

$$r=\min[r+floor(\eta\times i),k_3] \tag{23}$$

where η stands for the step size for updating rank r. Function $floor(\cdot)$ represents the round down operation. After each iteration, we check the convergence condition via:

$$\left\|\mathcal{Z}^{i+1}-\mathcal{B}^i\times_3\mathbf{A}^i\right\|_F / \left\|\mathcal{B}^i\times_3\mathbf{A}^i\right\|_F < \varepsilon \tag{24}$$

If current result meets this convergence condition, the denoised HSI $\mathcal{X}$ is finally output as:

$$\mathcal{X}=\mathcal{B}^{i+1}\times_3\mathbf{A}^{i+1} \tag{25}$$

Otherwise, we continuously perform the next alternating iterative optimization, until meeting the convergence condition or arriving the maximum iteration $i_{\max}$. The pseudocode of the proposed SLRP-DSP for HSI self-supervised denoising is depicted in Algorithm 1.

Algorithm 1 Alternating Iterative Optimization for the SLRP-DLP HSI Self-Supervised Denoising Method

Input: Noisy HSI $\mathcal{Y}\in\mathbb{R}^{k_1\times k_2\times k_3}$, Tucker rank r, parameters β, η, and ε

Initialization: $\mathcal{Z}^1=\mathcal{Y}$, $\mathcal{Q}^1=\mathbf{0}$, $r=4$, $\beta=0.1$,$\kappa=1.1$, $\eta=0.2$, $\varepsilon=1e-4$, $i=1$, $i_{\max}=40$, $p_{\max}=10$

while not converged and $i\le i_{\max}$ **do**
  Updating $\mathbf{A}^i$ via (8)
  Updating $\hat{\mathcal{B}}^i$ via (10)
  Updating $\mathcal{B}^i$ via (12)
  Initialization: $p=1$, $\mathcal{Z}_p^i=\mathop{\mathbb{S}}_{j=1}^{k_3}\langle Patch(\mathcal{Z}^i(:,:,j))\rangle$
  while $i>1$ and $p\le p_{\max}$ **do**
    Updating self-supervised loss of $\mathcal{T}_{DSP}$ via (14)
    self-supervised fine-tuning for $\mathcal{T}_{DSP}$ via (16)
    Updating $\mathcal{Z}_{p+1}^i=Sort\mathop{\mathbb{S}}_{j=1}^{k_3}\langle\mathcal{Z}_p^i(:,:,j)\rangle$
    If $\left\|\mathcal{T}_{DSP}(\mathcal{B}^i)-\mathcal{B}^i\right\|_F/\left\|\mathcal{B}^i\right\|_F<\varepsilon$, **stop**
    Let $p=p+1$
  end while
  Updating $\mathcal{P}^{i+1}$ via (20)
  Updating $\mathcal{Z}^{i+1}$ via (21)
  Updating β^{i+1} via (22)
  Updating Tucker rank $r=\min\langle r+floor(\eta\times i),k_3\rangle$
  If $\left\|\mathcal{Z}^{i+1}-\mathcal{B}^i\times_3\mathbf{A}^i\right\|_F/\left\|\mathcal{B}^i\times_3\mathbf{A}^i\right\|_F<\varepsilon$, **stop**
  Let $i=i+1$
end while

Output: The denoised result $\mathcal{X}=\mathcal{B}^{i+1}\times_3\mathbf{A}^{i+1}$

III. Experimental Results

In this section, we firstly give related parameters setting of the proposed SLRP-DSP method in Section III-A. Later, the simulated and real HSI denoising experiments are revealed in Section III-B and III-C, respectively.

A. Parameters Setting

In the proposed SLRP-DSP method, the initialized parameters of the alternating iterative optimization framework are listed in Algorithm 1. In addition, the related parameters setting of fine-tuning operation in deep spatial prior are given below. The patch size of the training samples in deep spatial prior is set as 40 × 40. The patch stride is denoted as 20 for training samples. The batch size is fixed as 128 to accelerate fine-tuning procedure. Stochastic gradient descent (SGD) strategy is utilized for updating the deep spatial prior. The learning rate σ is set as 0.001.

B. Simulated HSI Denoising Experiments

In our experiments, two noise-free HSIs are employed as the simulated data: Washington D.C. Mall HSI (outdoor data) and CAVE Toy HSI (indoor data). W. DC Mall data is comprised of 191 bands after discarding vapor absorption bands, from wavelength 401nm to 2473nm by HYDICE sensor. The testing W. DC Mall data is cropped with the size of 200 × 200 × 191 in the simulated experiments. CAVE Toy data is comprised of 31 bands from wavelength 400nm to 700nm by Cooled CCD camera. The testing CAVE Toy data is formatted with the size of 512 × 512 × 31 in the simulated experiments.

To validate the scene adaptation under multiple noisy environments, we simulate four different cases for both W. DC Mall and CAVE Toy HSI data sets. The specific

TABLE I
EVALUATION INDEXES OF THE SIMULATED EXPERIMENTS ON THE W. DC MALL DATA SET

Case	Index	TDL	BM4D	LRMR	3DTV	HyRes	NGMeet	QRNN3D	HSID	SSGN	Proposed
Case 1 SNR = 45dB	MPSNR	31.48	36.86	37.14	37.25	38.76	39.62	38.79	39.26	38.55	**42.48**
	MSSIM	0.951	0.969	0.978	0.983	0.986	0.989	0.988	0.985	0.987	**0.991**
	MSAM	7.168	4.257	4.361	4.694	3.252	3.794	3.581	3.662	3.458	**2.617**
Case 2 SNR = 34dB	MPSNR	24.32	27.69	29.42	29.63	30.42	31.68	30.35	26.74	28.86	**32.98**
	MSSIM	0.905	0.948	0.966	0.968	0.971	0.975	0.967	0.946	0.965	**0.983**
	MSAM	12.17	5.969	4.913	4.875	4.793	4.658	4.807	6.890	5.381	**4.017**
Case 3 SNR = 25dB	MPSNR	23.56	27.83	26.85	27.41	28.13	30.86	26.24	25.98	28.42	**32.74**
	MSSIM	0.887	0.951	0.946	0.949	0.951	0.969	0.945	0.934	0.958	**0.982**
	MSAM	12.43	5.872	6.833	6.780	5.472	5.197	6.798	7.021	5.636	**4.089**
Case 4 SNR = 16dB	MPSNR	21.97	25.94	25.37	26.42	27.01	29.79	25.87	24.16	27.68	**31.96**
	MSSIM	0.865	0.932	0.926	0.935	0.939	0.953	0.932	0.918	0.947	**0.974**
	MSAM	12.94	6.997	7.048	6.924	6.197	5.614	6.948	7.653	6.059	**4.583**

simulated operations of these four cases are described as follow:

Case 1 (i.i.d. Gaussian noise): Every band in these two HSIs is contaminated by i.i.d. Gaussian noise. For all the bands in HSI, the variance σ_i of simulated Gaussian noise is equal for each other (σ_i=30).

Case 2 (non-i.i.d. Gaussian noise): Every band in these two HSIs is contaminated by non-i.i.d. Gaussian noise. In terms of diverse bands, the variance of simulated Gaussian noise is unequal for each other ($\sigma_i \in [0, 75]$). And it obeys the stochastic probability distribution.

Case 3 (non-i.i.d. Gaussian noise + stripe noise): Based on Case 2, additive stripe noise is simulated in these two HSIs, which are simultaneously contaminated by non-i.i.d. noise. The imposed way of stripe noise follows [62] for different bands in W. DC Mall and CAVE Toy HSI data sets.

Case 4 (non-i.i.d. Gaussian noise + stripe noise + pepper noise): Based on Case 3, the additive pepper noise is simulated in these two HSIs, which are simultaneously contaminated by non-i.i.d. noise and stripe noise in Case 3. The simulated way of impulse noise follows [30] for different bands in the two HSI data sets.

Besides, nine classical HSI denoising algorithms are regarded as the comparison approaches, to validate the reliability of the proposed framework. These approaches include both model-driven methods: tensor dictionary learning (TDL) [26], non-local block matching 4D data denoising (BM4D) [16], low-rank matrix recovery (LRMR) [20], 3D total variation (3DTV) [15], HyRes [7], non-local meet global for HSI restoration (NGMeet) [63]. And data-driven methods: QRNN3D [47], HSI denoising convolution neural network (HSID-CNN) [43], spatio-spectral gradient network (SSGN) [44].

With respect to the quantitative evaluation index for HSI restoration, we employ three indexes in our simulated experiments: mean PSNR (MPSNR), mean SSIM (MSSIM), and mean SAM (MSAM). MPSNR and MSSIM are utilized for evaluating the spatial recovery degree in HSI denoising. MSAM is used for verifying the spectral perseveration degree in HSI denoising. Generally, the higher the MPSNR/MSSIM index and the lower MSA index are, the better the quality of HSI restoration is. As listed in Table I and II, MPSNR, MSSIM and MSA for each algorithm are given in the two simulated HSI data sets and four cases, respectively. For comparisons, the optimal index for every row is labeled as bold format in Table I and Table II.

a) W. DC Mall data set: Table I displays the three objective evaluation indexes (MPSNR, MSSIM and MSA) of nine contrast algorithms, under the four noisy cases for the W. DC Mall HSI data set. Besides, the pseudo-color denoising results of bands (57, 27, 17) in Case 3 are presented in Fig. 2. For better distinguishing the restoration quality, the enlarged figures for local details are also given in Fig. 2.

As shown in Table I, the proposed method outperforms on MPSNR, MSSIM and MSAM indexes compared with both model-driven HSI denoising methods (TDL, BM4D, LRMR, 3DTV, HyRes, and NGMeet) and data-driven HSI denoising methods (QRNN3D, HSID-CNN, and SSGN). In Case 3, the proposed model can effectively eliminate the mixed noise without obvious residual stripe noise in Fig. 2(l).

In addition, spectral preservation is extremely significant for HSI restoration. The spectral curves of position (78, 75) in W. DC HSI data set are also depicted in Fig. 3. For better comparisons, the original noise-free spectral curve is given in each denoising result through eight contrast methods and proposed method. As shown in Fig. 3(a)-(j), the presented SLRP-DSP model can preserve spectral information, compared with other HSI restoration methods.

b) CAVE Toy data set: Table II lists the three objective evaluation indexes (MPSNR, MSSIM and MSA) of nine contrast algorithms, under the four noisy cases for the CAVE

TABLE II
EVALUATION INDEXES OF THE SIMULATED EXPERIMENTS ON THE CAVE TOY DATA SET

Case	Index	TDL	BM4D	LRMR	3DTV	HyRes	NGMeet	QRNN3D	HSID	SSGN	Proposed
Case 1 SNR = 46dB	MPSNR	33.59	37.83	37.21	38.19	40.63	43.47	39.25	38.34	39.76	**45.19**
	MSSIM	0.916	0.967	0.963	0.975	0.978	0.989	0.971	0.974	0.982	**0.990**
	MSAM	9.648	5.742	6.039	5.247	4.839	3.476	4.951	5.182	4.153	**2.576**
Case 2 SNR = 38dB	MPSNR	23.67	32.42	28.76	30.68	30.85	33.24	29.49	27.56	30.21	**35.39**
	MSSIM	0.814	0.946	0.914	0.933	0.937	0.951	0.926	0.863	0.938	**0.967**
	MSAM	19.98	8.374	14.56	10.89	10.64	7.278	11.45	16.49	10.46	**5.482**
Case 3 SNR = 27dB	MPSNR	22.86	29.25	26.83	29.92	30.03	32.34	28.95	25.71	30.66	**34.98**
	MSSIM	0.819	0.914	0.887	0.911	0.917	0.945	0.903	0.842	0.929	**0.961**
	MSAM	20.66	12.75	15.06	11.69	11.32	8.028	12.25	17.36	9.147	**5.834**
Case 4 SNR = 18dB	MPSNR	21.97	25.94	25.37	26.46	27.01	29.79	26.03	24.16	27.68	**31.96**
	MSSIM	0.805	0.912	0.886	0.904	0.907	0.937	0.901	0.838	0.927	**0.954**
	MSAM	22.94	12.98	15.34	11.92	11.56	8.248	12.49	17.65	9.439	**6.183**

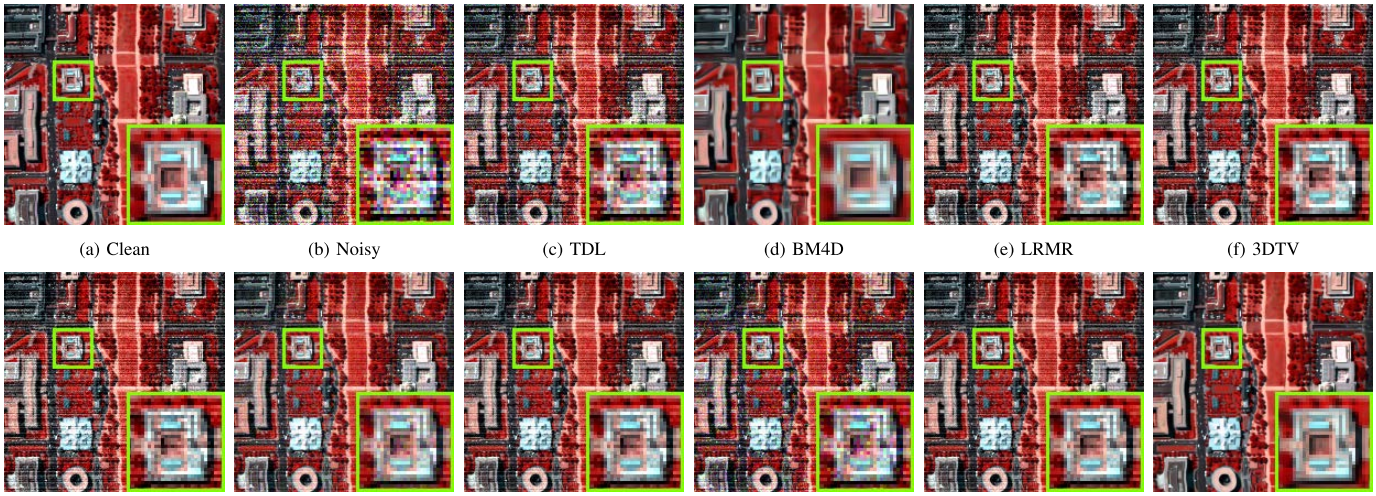

(a) Clean (b) Noisy (c) TDL (d) BM4D (e) LRMR (f) 3DTV

(g) HyRes (h) NGMeet (i) QRNN3D (j) HSID-CNN (k) SSGN (l) Proposed

Fig. 2. Simulated denoising results for bands (57, 27, 17) of W. DC Mall HSI in Case 3.

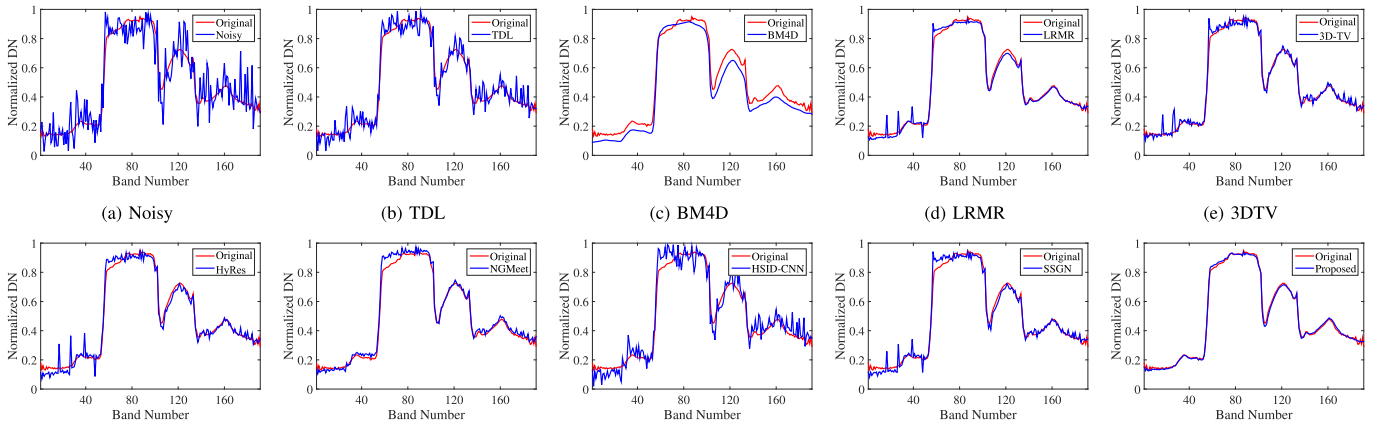

(a) Noisy (b) TDL (c) BM4D (d) LRMR (e) 3DTV

(f) HyRes (g) NGMeet (h) HSID-CNN (i) SSGN (j) Proposed

Fig. 3. Spectral curves for position (78, 75) of W. DC Mall HSI in Case 3.

Toy HSI data set. Besides, the denoising results of 26th-band in Case 2 are presented in Fig. 4. For better distinguishing the restoration quality, the enlarged figures for local details are also portrayed in Fig. 4.

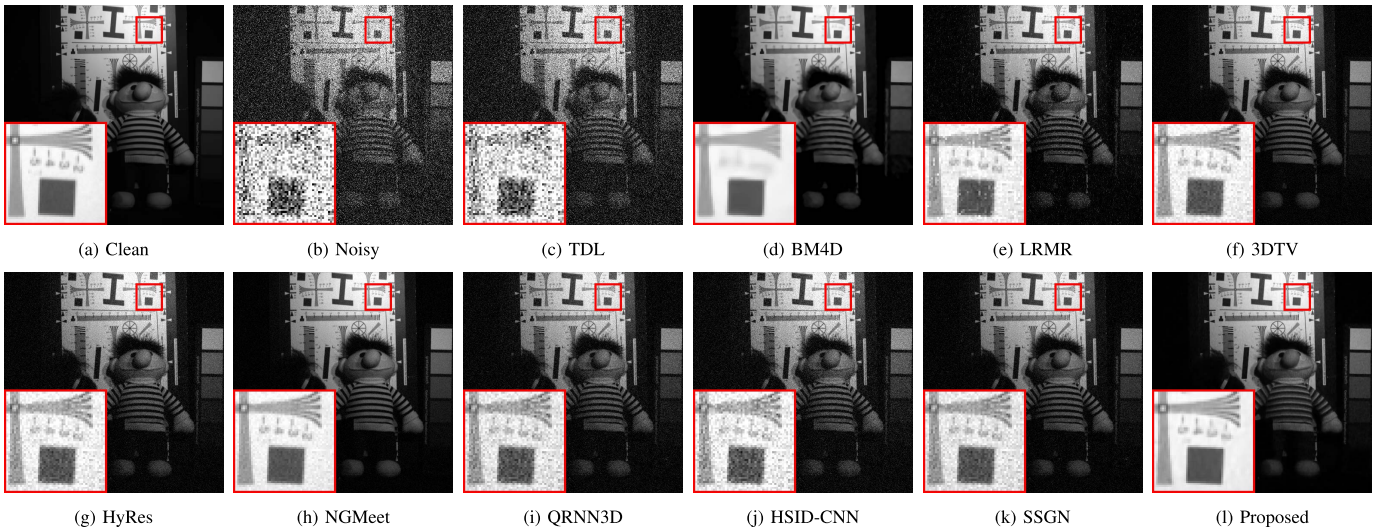

(a) Clean (b) Noisy (c) TDL (d) BM4D (e) LRMR (f) 3DTV

(g) HyRes (h) NGMeet (i) QRNN3D (j) HSID-CNN (k) SSGN (l) Proposed

Fig. 4. Simulated denoising results for 26-th band of CAVE Toy HSI in Case 2.

TABLE III
BLIND QUALITY ASSESSMENT USING Q-METRIC IN THE REAL HSI DENOISING EXPERIMENTS

Data Set	TDL	BM4D	LRMR	3DTV	NMoG	HyRes	NGMeet	QRNN3D	HSID	SSGN	Proposed
Urban	0.041	0.064	0.061	0.068	0.072	0.071	0.069	0.067	0.065	0.068	**0.076**
Indian	0.053	0.071	0.075	0.083	0.079	0.082	0.083	0.078	0.076	0.082	**0.086**
GF-5	0.038	0.042	0.052	0.045	0.060	0.053	0.048	0.047	0.046	0.053	**0.064**
Zhuhai-1	0.042	0.047	0.061	0.063	0.058	0.061	0.065	0.062	0.059	0.063	**0.070**

TABLE IV
RUNNING-TIMES OF DIFFERENT HSI DENOISING METHODS IN THE REAL EXPERIMENTS (UNIT: SECOND)

Data Set	TDL	BM4D	LRMR	3DTV	NMoG	HyRes	NGMeet	QRNN3D	HSID	SSGN	Proposed
Urban	713.8	936.2	1155.6	789.4	1325.4	867.3	452.4	24.9	**8.7**	15.6	63.2
Indian	184.1	236.3	268.7	195.8	348.2	297.3	137.8	8.2	**2.6**	3.9	44.7
GF-5	993.4	1085.7	1723.5	1034.1	1297.6	1138.5	893.9	38.6	**15.4**	21.4	96.3
Zhuhai-1	139.6	156.2	184.3	147.8	261.9	185.7	64.5	9.4	**2.2**	3.1	36.7

As shown in Table II, the proposed method outperforms on MPSNR, MSSIM, and MSAM indexes compared with both model-driven methods (TDL, BM4D, LRMR, 3DTV, HyRes, and NGMeet) and data-driven methods (QRNN3D, HSID-CNN, and SSGN). Besides, the proposed SLRP-DSP can simultaneously remove random noise and reduce residual artifacts in Fig. 4(l). And the spatial details are also clearly recovered especially for the tiny textures in CAVE Toy. In comparisons, other contrast methods exist residual noise, or blurry issue, to different degree.

C. Real HSI Denoising Experiments

To further testify the reliability and adaptation of the presented SLRP-DSP, four real noisy HSI data sets are employed in our experiments: Urban ($307 \times 307 \times 188$), Indian Pines ($145 \times 145 \times 206$), GF-5 ($400 \times 400 \times 330$), and Zhuhai-1 ($400 \times 400 \times 32$). It should be highlighted that these noisy HSIs exist large diversity on spatial resolution, spectral resolution, spectral range, and scene types. And the noise levels and types are also different between each other.

Ten HSI denoising algorithms: TDL, BM4D, LRMR, 3DTV, NMoG, HyRes, NGMeet, QRNN3D, HSID-CNN, and SSGN are employed as contrasted methods. For effectively distinguishing the restoration quality, the enlarged figures for local details are also given in each result. The blind quality index Q-Metrics of the four noisy HSIs are recorded in Table III. Meanwhile, the running-times of above methods in the real experiments are listed in Table IV. The optimal index is marked as bold format. The concrete results and analysis are described as follow:

1) Urban data set: As shown in Fig. 5, the denoising results for bands (187, 104, 24) of Urban HSI data set are listed through ten contrast methods and proposed method. This data set is polluted by mixed noise, included both random noise and

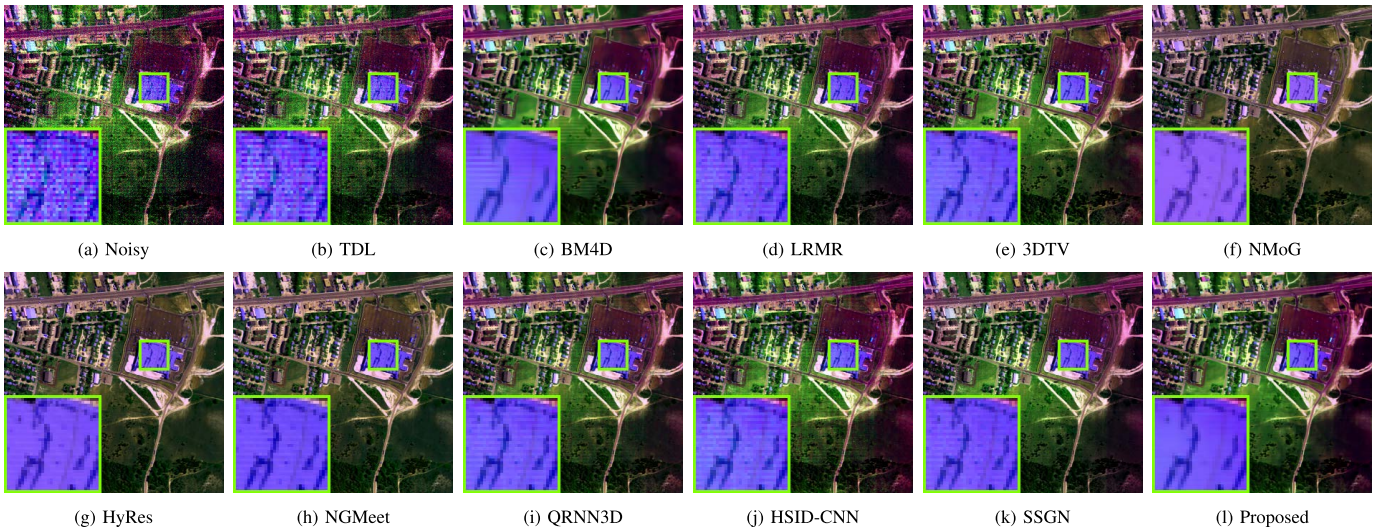

(a) Noisy (b) TDL (c) BM4D (d) LRMR (e) 3DTV (f) NMoG

(g) HyRes (h) NGMeet (i) QRNN3D (j) HSID-CNN (k) SSGN (l) Proposed

Fig. 5. Real denoising results for bands (187, 104, 24) of Urban HSI.

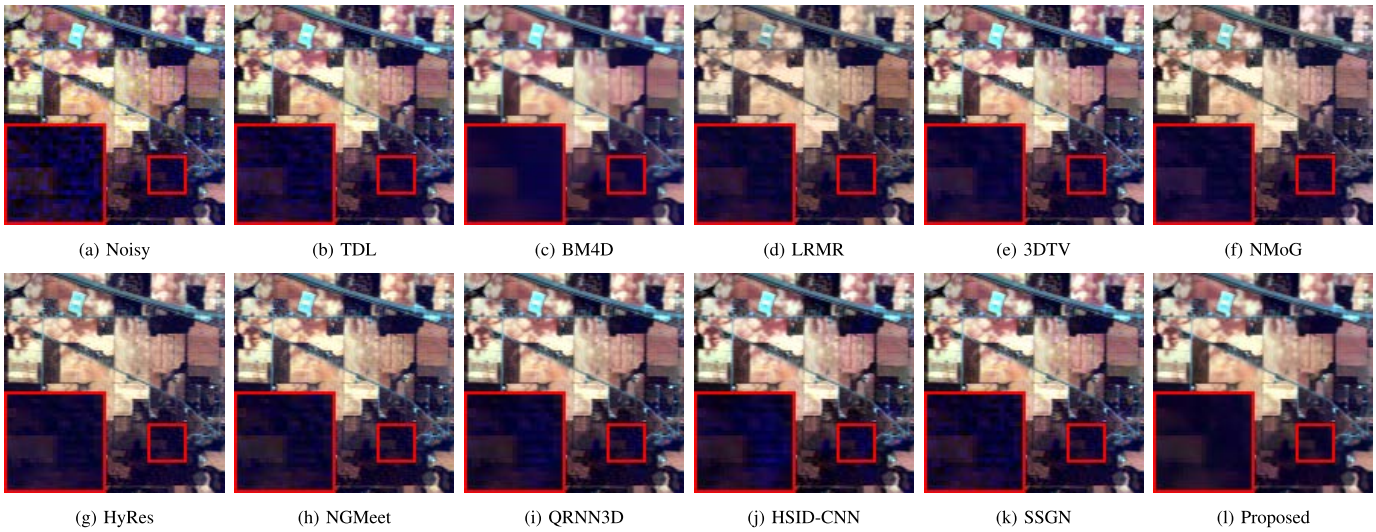

(a) Noisy (b) TDL (c) BM4D (d) LRMR (e) 3DTV (f) NMoG

(g) HyRes (h) NGMeet (i) QRNN3D (j) HSID-CNN (k) SSGN (l) Proposed

Fig. 6. Real denoising results for bands (145, 24, 2) of Indian Pines HSI.

stripe noise. Especially for magnified regions, the presented SLRP-DSP model outperforms on mixed noise removal and spectral information preservation. While other methods exist obvious residual stripe or spectral distortion in Fig. 5(b)-(k), to different degree.

2) Indian Pines data set: As displayed in Fig. 6, the denoising results for bands (145, 24, 2) of Indian Pines HSI data set are listed through ten contrast methods and proposed method. This HSI is mainly polluted by impulse noise. Especially for the magnified regions, the proposed SLRP-DSP method outperforms on impulse noise removal and spectral information preservation. While other methods exist obvious residual noise or spectral distortion in Fig. 6(b)-(k), especially for deep learning-based method.

3) GF-5 data set: As depicted in Fig. 7, the denoising results for 193-th band of GF-5 HSI are listed through ten contrast methods and proposed method. This data set is mainly polluted by mixed noise, included both random noise and stripe noise. Compared with these HSI denoising methods, the proposed framework outperforms on mixed noise removal and spatial details recovery. While other methods generate plenty of spatial artifacts in Fig. 7(b)-(k).

TABLE V
ABLATION ANALYSIS ON FINE-TUNING STRATEGY

Index	With Fine-tuning	Without Fine-tuning
MPSNR	**32.74**	30.56
MSSIM	**0.982**	0.967
MSA	**4.089**	5.323

4) Zhuhai-1 data set: As shown in Fig. 8, the denoising results for 32-th band of Zhuhai-1 HSI data set are listed through ten contrast methods and proposed method. This data set is mainly polluted by random noise. Especially for the magnified regions, the proposed SLRP-DSP method

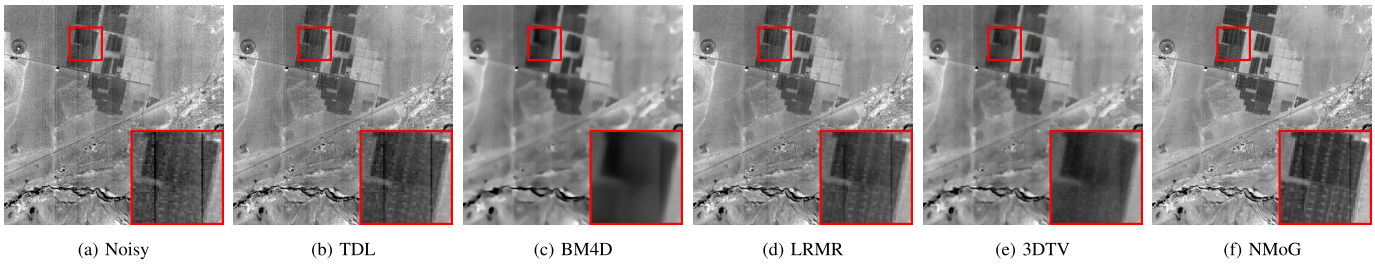

(a) Noisy (b) TDL (c) BM4D (d) LRMR (e) 3DTV (f) NMoG

(g) HyRes (h) NGMeet (i) QRNN3D (j) HSID-CNN (k) SSGN (l) Proposed

Fig. 7. Real denoising results for 193-th band of GF-5 HSI.

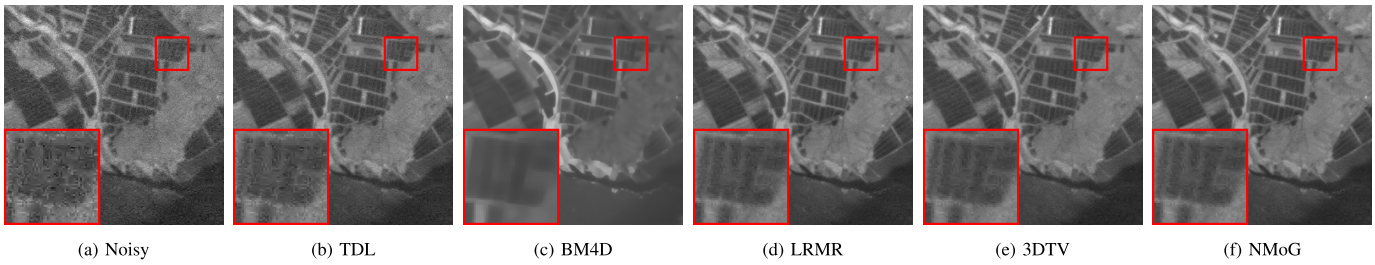

(a) Noisy (b) TDL (c) BM4D (d) LRMR (e) 3DTV (f) NMoG

(g) HyRes (h) NGMeet (i) QRNN3D (j) HSID-CNN (k) SSGN (l) Proposed

Fig. 8. Real denoising results for 32-th band of Zhuhai-1 HSI.

TABLE VI

PERFORMANCE OF THE PROPOSED AND COMPARED METHODS UNDER DIFFERENT NOISE LEVELS (SAME NOISE)

Noise Level	Index	Noisy	TDL	BM4D	LRMR	3DTV	NMoG	NGMeet	HSID	SSGN	Proposed
σ_i=30	MPSNR	21.38	27.56	29.72	31.85	32.16	33.98	34.27	33.86	33.91	**35.24**
	MSSIM	0.752	0.928	0.948	0.969	0.972	0.983	0.986	0.981	0.982	**0.989**
	MSAM	19.64	9.043	5.976	5.423	5.383	4.006	3.842	4.025	4.013	**3.576**
σ_i=60	MPSNR	17.64	23.89	27.45	29.16	29.93	30.11	30.52	31.64	31.78	**33.92**
	MSSIM	0.631	0.875	0.903	0.946	0.948	0.952	0.953	0.962	0.964	**0.978**
	MSAM	23.74	13.35	7.182	6.859	6.667	5.435	4.728	4.936	4.895	**4.013**
σ_i=90	MPSNR	12.58	19.46	24.25	25.67	25.81	28.36	28.84	29.53	29.96	**31.74**
	MSSIM	0.603	0.714	0.825	0.902	0.911	0.924	0.933	0.948	0.950	**0.967**
	MSAM	25.18	16.79	9.965	8.724	7.933	7.018	6.145	6.022	5.974	**5.208**

outperforms on random noise removal and spatial details recovery. Compared with both model-driven and data driven HSI denoising methods, these experimental results magnifest the credibility and availability of the proposed SLRP-DSP.

IV. Discussions

A. Ablation Analysis

In the proposed SLRP-DSP method, the self-supervised fine-tuning strategy is utilized to adjust the convolutional parameters in DnCNN model. Therefore, we need discuss the significance of fine-tuning strategy for DnCNN. As listed in Table V, the proposed method with fine-tuning strategy and without fine-tuning for DnCNN are compared in the same experiment (W.DC Mall, Case 3). Through the fine-tuning strategy, the proposed method could adaptively adjust the deep spatial denoiser for each noisy HSI. Table V demonstrates the effectiveness of this fine-tuning strategy for HSI denoising.

B. Noise Level Analysis

To validate the performance of the proposed method and the compared methods under different noise levels of the same noise, we simulate three different noisy scenes for W. DC Mall HSI. The simulated operation is described as follow: Every band in this HSI is contaminated by the same noise (i.i.d. Gaussian noise). For all the bands in HSI, the variance σ_i of simulated Gaussian noise is equal to 30, 60 and 90. As listed in Table VI, the proposed method outperforms on MPSNR, MSSIM and MSAM indexes compared with both model-driven HSI denoising methods (TDL, BM4D, LRMR, 3DTV, NMoG, and NGMeet) and data-driven HSI denoising methods (HSID-CNN and SSGN). This discussion manifests the stability of the proposed method under different noise levels.

V. Conclusion

In this work, we develop a self-supervised HSI denoising method via integrating model-driven strategy with data-driven strategy. The proposed framework simultaneously cooperates the spectral low-rankness prior and deep spatial prior (SLRP-DSP) for HSI self-supervised denoising. Through this strategy, SLRP-DSP can both exploit the internal low-rankness prior of third-order tensor and the spatial feature extraction capacity of CNN, without plenty of clean HSI training samples. Experimental results demonstrate that the proposed SLRP-DSP outperforms on mixed noise removal in different HSIs.

In our future work, we will exploit more strategy via combing data-driven with model-driven for HSI denoising. Besides, how to better utilize the low-rankness prior in joint spectral and spatial dimension of HSI is also the crucial point for HSI denoising.

References

[1] J. M. Bioucas-Dias, A. Plaza, G. Camps-Valls, P. Scheunders, N. M. Nasrabadi, and J. Chanussot, "Hyperspectral remote sensing data analysis and future challenges," *IEEE Geosci. Remote Sens. Mag.*, vol. 1, no. 2, pp. 6–36, Jun. 2013.

[2] F. Xiong, J. Zhou, and Y. Qian, "Material based object tracking in hyperspectral videos," *IEEE Trans. Image Process.*, vol. 29, pp. 3719–3733, 2020.

[3] M. E. Paoletti, J. M. Haut, J. Plaza, and A. Plaza, "Deep learning classifiers for hyperspectral imaging: A review," *ISPRS J. Photogramm. Remote Sens.*, vol. 158, pp. 279–317, Dec. 2019.

[4] R. Arablouei and F. de Hoog, "Hyperspectral image recovery via hybrid regularization," *IEEE Trans. Image Process.*, vol. 25, no. 12, pp. 5649–5663, Dec. 2016.

[5] B. Lin, X. Tao, and J. Lu, "Hyperspectral image denoising via matrix factorization and deep prior regularization," *IEEE Trans. Image Process.*, vol. 29, pp. 565–578, 2020.

[6] J. M. Bioucas-Dias and J. M. P. Nascimento, "Hyperspectral subspace identification," *IEEE Trans. Geosci. Remote Sensing*, vol. 46, no. 8, pp. 2435–2445, Aug. 2008.

[7] B. Rasti, "Sparse hyperspectral image modeling and restoration," Ph.D. dissertation, Dept. Elect. Comput. Eng., Univ. Iceland, Reykjavik, Iceland, 2014.

[8] D. Coquelin, B. Rasti, M. Götz, P. Ghamisi, R. Gloaguen, and A. Streit, "HyDe: The first open-source, Python-based, GPU-accelerated hyperspectral denoising package," 2022, *arXiv:2204.06979*.

[9] N. Renard, S. Bourennane, and J. Blanc-Talon, "Denoising and dimensionality reduction using multilinear tools for hyperspectral images," *IEEE Trans. Geosci. Remote Sens.*, vol. 5, no. 2, pp. 138–142, May 2008.

[10] W. Dong et al., "Hyperspectral image super-resolution via non-negative structured sparse representation," *IEEE Trans. Image Process.*, vol. 25, no. 5, pp. 2337–2352, May 2016.

[11] B. Rasti, P. Scheunders, P. Ghamisi, G. Licciardi, and J. Chanussot, "Noise reduction in hyperspectral imagery: Overview and application," *Remote Sens.*, vol. 10, no. 3, p. 482, Oct. 2018.

[12] B. Rasti, Y. Chang, E. Dalsasso, L. Denis, and P. Ghamisi, "Image restoration for remote sensing: Overview and toolbox," *IEEE Geosci. Remote Sens. Mag.*, vol. 10, no. 2, pp. 1–31, Nov. 2021.

[13] H. K. Aggarwal and A. Majumdar, "Hyperspectral image denoising using spatio-spectral total variation," *IEEE Geosci. Remote Sens. Lett.*, vol. 13, no. 3, pp. 442–446, Mar. 2016.

[14] Y. Chen, J. Li, and Y. Zhou, "Hyperspectral image denoising by total variation-regularized bilinear factorization," *Signal Process.*, vol. 174, Sep. 2020, Art. no. 107645.

[15] J. Peng, Q. Xie, Q. Zhao, Y. Wang, L. Yee, and D. Meng, "Enhanced 3DTV regularization and its applications on HSI denoising and compressed sensing," *IEEE Trans. Image Process.*, vol. 29, pp. 7889–7903, 2020.

[16] M. Maggioni, V. Katkovnik, K. Egiazarian, and A. Foi, "Nonlocal transform-domain filter for volumetric data denoising and reconstruction," *IEEE Trans. Image Process.*, vol. 22, no. 1, pp. 119–133, Jan. 2013.

[17] Y.-Q. Zhao and J. Yang, "Hyperspectral image denoising via sparse representation and low-rank constraint," *IEEE Trans. Geosci. Remote Sens.*, vol. 53, no. 1, pp. 296–308, Jan. 2015.

[18] Y. Chen, W. He, N. Yokoya, and T.-Z. Huang, "Hyperspectral image restoration using weighted group sparsity-regularized low-rank tensor decomposition," *IEEE Trans. Cybern.*, vol. 50, no. 8, pp. 3556–3570, Aug. 2020.

[19] L. Zhuang and J. M. Bioucas-Dias, "Fast hyperspectral image denoising and inpainting based on low-rank and sparse representations," *IEEE J. Sel. Topics Appl. Earth Observ. Remote Sens.*, vol. 11, no. 3, pp. 730–742, Mar. 2018.

[20] H. Zhang, W. He, L. Zhang, H. Shen, and Q. Yuan, "Hyperspectral image restoration using low-rank matrix recovery," *IEEE Trans. Geosci. Remote Sens.*, vol. 52, no. 8, pp. 4729–4743, Aug. 2014.

[21] W. He, H. Zhang, L. Zhang, and H. Shen, "Total-variation-regularized low-rank matrix factorization for hyperspectral image restoration," *IEEE Trans. Geosci. Remote Sens.*, vol. 54, no. 1, pp. 178–188, Jan. 2016.

[22] Q. Xie, Q. Zhao, D. Meng, and Z. Xu, "Kronecker-basis-representation based tensor sparsity and its applications to tensor recovery," *IEEE Trans. Pattern Anal. Mach. Intell.*, vol. 40, no. 8, pp. 1888–1902, Aug. 2018.

[23] T. Xie, S. Li, and B. Sun, "Hyperspectral images denoising via nonconvex regularized low-rank and sparse matrix decomposition," *IEEE Trans. Image Process.*, vol. 29, pp. 44–56, 2020.

[24] X.-L. Zhao, H. Zhang, T.-X. Jiang, M. K. Ng, and X.-J. Zhang, "Fast algorithm with theoretical guarantees for constrained low-tubal-rank tensor recovery in hyperspectral images denoising," *Neurocomputing*, vol. 413, pp. 397–409, Nov. 2020.

[25] Y. Zheng, T. Huang, X. Zhao, Y. Chen, and W. He, "Double-factor-regularized low-rank tensor factorization for mixed noise removal in hyperspectral image," *IEEE Trans. Geosci. Remote Sens.*, vol. 58, no. 12, pp. 8450–8464, Dec. 2020.

[26] Y. Peng, D. Meng, Z. Xu, C. Gao, Y. Yang, and B. Zhang, "Decomposable nonlocal tensor dictionary learning for multispectral image denoising," in *Proc. IEEE Conf. Comput. Vis. Pattern Recognit.*, Jun. 2014, pp. 2949–2956.

[27] C. Lu, J. Feng, Y. Chen, W. Liu, Z. Lin, and S. Yan, "Tensor robust principal component analysis with a new tensor nuclear norm," *IEEE Trans. Pattern Anal. Mach. Intell.*, vol. 42, no. 4, pp. 925–938, Apr. 2020.

[28] H. Fan, C. Li, Y. Guo, G. Kuang, and J. Ma, "Spatial–spectral total variation regularized low-rank tensor decomposition for hyperspectral image denoising," *IEEE Trans. Geosci. Remote Sens.*, vol. 56, no. 10, pp. 6196–6213, Oct. 2018.

[29] F. Xiong, J. Zhou, and Y. Qian, "Hyperspectral restoration via L_0 gradient regularized low-rank tensor factorization," *IEEE Trans. Geosci. Remote Sens.*, vol. 57, no. 12, pp. 10410–10425, Dec. 2019.

[30] Y.-B. Zheng, T.-Z. Huang, X.-L. Zhao, T.-X. Jiang, T.-H. Ma, and T.-Y. Ji, "Mixed noise removal in hyperspectral image via low-fibered-rank regularization," *IEEE Trans. Geosci. Remote Sens.*, vol. 58, no. 1, pp. 734–749, Jan. 2020.

[31] M. Zhang, W. Li, and Q. Du, "Diverse region-based CNN for hyperspectral image classification," *IEEE Trans. Image Process.*, vol. 27, no. 6, pp. 2623–2634, Jun. 2018.

[32] Y. Fu, Y. Zheng, H. Huang, I. Sato, and Y. Sato, "Hyperspectral image super-resolution with a mosaic RGB image," *IEEE Trans. Image Process.*, vol. 27, no. 11, pp. 5539–5552, Nov. 2018.

[33] J. Liu, W. Yang, S. Yang, and Z. Guo, "D3R-Net: Dynamic routing residue recurrent network for video rain removal," *IEEE Trans. Image Process.*, vol. 28, no. 2, pp. 699–712, Feb. 2019.

[34] K. Zhang, W. Zuo, Y. Chen, D. Meng, and L. Zhang, "Beyond a Gaussian Denoiser: Residual learning of deep CNN for image denoising," *IEEE Trans. Image Process.*, vol. 26, no. 7, pp. 3142–3155, Jul. 2017.

[35] C. Dong, C. C. Loy, K. He, and X. Tang, "Image super-resolution using deep convolutional networks," *IEEE Trans. Pattern Anal. Mach. Intell.*, vol. 38, no. 2, pp. 295–307, Feb. 2016.

[36] Q. Zhang, Q. Yuan, C. Zeng, X. Li, and Y. Wei, "Missing data reconstruction in remote sensing image with a unified spatial–temporal–spectral deep convolutional neural network," *IEEE Trans. Geosci. Remote Sens.*, vol. 56, no. 8, pp. 4274–4288, Aug. 2018.

[37] Q. Zhang, Q. Yuan, J. Li, Z. Li, H. Shen, and L. Zhang, "Thick cloud and cloud shadow removal in multitemporal imagery using progressively spatio–temporal patch group deep learning," *ISPRS J. Photogramm. Remote Sens.*, vol. 162, pp. 148–160, Apr. 2020.

[38] Q. Zhang, Q. Yuan, Z. Li, F. Sun, and L. Zhang, "Combined deep prior with low-rank tensor SVD for thick cloud removal in multitemporal images," *ISPRS J. Photogramm. Remote Sens.*, vol. 177, pp. 161–173, Jul. 2021.

[39] R. Dian, S. Li, A. Guo, and L. Fang, "Deep hyperspectral image sharpening," *IEEE Trans. Neural Netw. Learn. Syst.*, vol. 29, no. 11, pp. 5345–5355, Nov. 2018.

[40] R. Dian and S. Li, "Hyperspectral image super-resolution via subspace-based low tensor multi-rank regularization," *IEEE Trans. Image Process.*, vol. 28, no. 10, pp. 5135–5146, Oct. 2019.

[41] L. Zhang, J. Nie, W. Wei, Y. Li, and Y. Zhang, "Deep blind hyperspectral image super-resolution," *IEEE Trans. Neural Netw. Learn. Syst.*, vol. 32, no. 6, pp. 2388–2400, Jun. 2021.

[42] W. Xie and Y. Li, "Hyperspectral imagery denoising by deep learning with trainable nonlinearity function," *IEEE Geosci. Remote Sens. Lett.*, vol. 14, no. 11, pp. 1963–1967, Nov. 2017.

[43] Q. Yuan, Q. Zhang, J. Li, H. Shen, and L. Zhang, "Hyperspectral image denoising employing a spatial–spectral deep residual convolutional neural network," *IEEE Trans. Geosci. Remote Sens.*, vol. 57, no. 2, pp. 1205–1218, Feb. 2019.

[44] Q. Zhang, Q. Yuan, J. Li, X. Liu, H. Shen, and L. Zhang, "Hybrid noise removal in hyperspectral imagery with a spatial–spectral gradient network," *IEEE Trans. Geosci. Remote Sens.*, vol. 57, no. 10, pp. 7317–7329, Oct. 2019.

[45] Y. Chang, L. Yan, H. Fang, S. Zhong, and W. Liao, "HSI-DeNet: Hyperspectral image restoration via convolutional neural network," *IEEE Trans. Geosci. Remote Sens.*, vol. 57, no. 2, pp. 667–682, Feb. 2019.

[46] W. Dong, H. Wang, F. Wu, G. M. Shi, and X. Li, "Deep spatial–spectral representation learning for hyperspectral image denoising," *IEEE Trans. Comput. Imag.*, vol. 5, no. 4, pp. 635–648, Dec. 2019.

[47] K. Wei, Y. Fu, and H. Huang, "3-D quasi-recurrent neural network for hyperspectral image denoising," *IEEE Trans. Neural Netw. Learn. Syst.*, vol. 32, no. 1, pp. 363–375, Jan. 2021.

[48] Q. Zhang, Q. Yuan, J. Li, F. Sun, and L. Zhang, "Deep spatio-spectral Bayesian posterior for hyperspectral image non-i.i.d. noise removal," *ISPRS J. Photogramm. Remote Sens.*, vol. 164, pp. 125–137, Jun. 2020.

[49] A. Maffei, J. M. Haut, M. E. Paoletti, J. Plaza, L. Bruzzone, and A. Plaza, "A single model CNN for hyperspectral image denoising," *IEEE Trans. Geosci. Remote Sens.*, vol. 58, no. 4, pp. 2516–2529, Apr. 2020.

[50] H. V. Nguyen, M. O. Ulfarsson, and J. R. Sveinsson, "Hyperspectral image denoising using SURE-based unsupervised convolutional neural networks," *IEEE Trans. Geosci. Remote Sens.*, vol. 59, no. 4, pp. 3369–3382, Apr. 2021.

[51] H. Zhang, H. Chen, G. Yang, and L. Zhang, "LR-Net: Low-rank spatial–spectral network for hyperspectral image denoising," *IEEE Trans. Image Process.*, vol. 30, pp. 8743–8758, 2021.

[52] M. Ye, Y. Qian, and J. Zhou, "Multitask sparse nonnegative matrix factorization for joint spectral–spatial hyperspectral imagery denoising," *IEEE Trans. Geosci. Remote Sens.*, vol. 53, no. 5, pp. 2621–2639, May 2015.

[53] Q. Zhang, Q. Yuan, J. Li, Z. Yang, and X. Ma, "Learning a dilated residual network for SAR image despeckling," *Remote Sens.*, vol. 10, no. 2, p. 196, Feb. 2018.

[54] W. Liu and J. Lee, "A 3-D atrous convolution neural network for hyperspectral image denoising," *IEEE Trans. Geosci. Remote Sens.*, vol. 57, no. 8, pp. 5701–5715, Aug. 2019.

[55] S. Guo, Z. Liang, and L. Zhang, "Joint denoising and demosaicking with green channel prior for real-world burst images," *IEEE Trans. Image Process.*, vol. 30, pp. 6930–6942, 2021.

[56] T. G. Kolda and B. W. Bader, "Tensor decompositions and applications," *SIAM Rev.*, vol. 51, no. 3, pp. 455–500, Sep. 2009.

[57] N. D. Sidiropoulos, L. De Lathauwer, X. Fu, K. Huang, E. E. Papalexakis, and C. Faloutsos, "Tensor decomposition for signal processing and machine learning," *IEEE Trans. Signal Process.*, vol. 65, no. 13, pp. 3551–3582, Jul. 2017.

[58] C. Lu, J. Feng, Z. Lin, T. Mei, and S. Yan, "Subspace clustering by block diagonal representation," *IEEE Trans. Pattern Anal. Mach. Intell.*, vol. 41, no. 2, pp. 487–501, Feb. 2019.

[59] X. Gong, W. Chen, and J. Chen, "A low-rank tensor dictionary learning method for hyperspectral image denoising," *IEEE Trans. Signal Process.*, vol. 68, pp. 1168–1180, 2020.

[60] Y. Chang, L. Yan, X. Zhao, H. Fang, Z. Zhang, and S. Zhong, "Weighted low-rank tensor recovery for hyperspectral image restoration," *IEEE Trans. Cybern.*, vol. 50, no. 11, pp. 4558–4572, Nov. 2020.

[61] B. Rasti, J. R. Sveinsson, and M. O. Ulfarsson, "Wavelet-based sparse reduced-rank regression for hyperspectral image restoration," *IEEE Trans. Geosci. Remote Sens.*, vol. 52, no. 10, pp. 6688–6698, Oct. 2014.

[62] Y. Chang, L. Yan, H. Fang, and C. Luo, "Anisotropic spectral-spatial total variation model for multispectral remote sensing image destriping," *IEEE Trans. Image Process.*, vol. 24, no. 6, pp. 1852–1866, Jun. 2015.

[63] W. He et al., "Non-local meets global: An integrated paradigm for hyperspectral image restoration," *IEEE Trans. Pattern Anal. Mach. Intell.*, vol. 44, no. 1, pp. 2089–2107, Apr. 2022.

Qiang Zhang received the B.E. degree in surveying and mapping engineering and the M.E. and Ph.D. degrees in photogrammetry and remote sensing from Wuhan University, Wuhan, China, in 2017, 2019, and 2022, respectively.

He is currently an Associate Professor with the Center of Hyperspectral Imaging in Remote Sensing (CHIRS), Information Science and Technology College, Dalian Maritime University. His research interests include remote sensing information processing, computer vision, and machine learning. He has published more than ten journal articles in *Earth System Science Data* (ESSD), *ISPRS Journal of Photogrammetry and Remote Sensing* (P&RS), and IEEE TRANSACTIONS ON GEOSCIENCE AND REMOTE SENSING. More details could be found at https://qzhang95.github.io.

Qiangqiang Yuan (Member, IEEE) received the B.S. degree in surveying and mapping engineering and the Ph.D. degree in photogrammetry and remote sensing from Wuhan University, Wuhan, China, in 2006 and 2012, respectively.

In 2012, he joined the School of Geodesy and Geomatics, Wuhan University, where he is currently a Professor. He has published more than 90 research papers, including more than 70 peer-reviewed articles in international journals, such as the *Remote Sensing of Environment*, *ISPRS Journal of Photogrammetry and Remote Sensing*, IEEE TRANSACTIONS ON IMAGE PROCESSING, and IEEE TRANSACTIONS ON GEOSCIENCE AND REMOTE SENSING. He has frequently served as a referee for more than 50 international journals for remote sensing and image processing. His current research interests include image reconstruction, remote sensing, image processing and application, and data fusion. He was a recipient of the Youth Talent Support Program of China in 2019, the Top-Ten Academic Star of Wuhan University in 2011, and the recognition of Best Reviewers of the IEEE GEOSCIENCE AND REMOTE SENSING LETTERS in 2019. In 2014, he also received the Hong Kong Scholar Award from the Society of Hong Kong Scholars and the China National Postdoctoral Council. He is on the editor board of eight international journals.

Meiping Song (Member, IEEE) received the Ph.D. degree from the College of Computer Science and Technology, Harbin Engineering University, Harbin, China, in 2006.

She has been a Professor with the College of Information Science and Technology, Dalian Maritime University, Dalian, China, since 2020. Her research interests include remote sensing and hyperspectral image processing.

Haoyang Yu (Member, IEEE) received the B.S. degree in information and computing science from Northeastern University, Shenyang, China, in 2013, and the Ph.D. degree in cartography and geographic information system from the Key Laboratory of Digital Earth Science, Aerospace Information Research Institute, Chinese Academy of Sciences (CAS), Beijing, China, in 2019.

He is currently an Associate Professor with the Center of Hyperspectral Imaging in Remote Sensing (CHIRS), Information Science and Technology College, Dalian Maritime University. His research interests include models and algorithms for hyperspectral image processing, analysis, and applications.

Liangpei Zhang (Fellow, IEEE) received the B.S. degree in physics from Hunan Normal University, Changsha, China, in 1982, the M.S. degree in optics from the Xi'an Institute of Optics and Precision Mechanics, Chinese Academy of Sciences, Xi'an, China, in 1988, and the Ph.D. degree in photogrammetry and remote sensing from Wuhan University, Wuhan, China, in 1998.

He was the Head of the State Key Laboratory of Information Engineering in Surveying, Mapping, and Remote Sensing (LIESMARS), Remote Sensing Division, Wuhan University. From 2011 to 2016, he was a Principal Scientist with the China State Key Basic Research Project, appointed by the Ministry of National Science and Technology of China to lead the remote sensing program in China. He is currently a Professor in the State Key Laboratory of Information Engineering in Surveying, Mapping and Remote Sensing, Wuhan University. His research interests include hyperspectral remote sensing, high-resolution remote sensing, image processing, and artificial intelligence.

Dr. Zhang is a fellow of the Institution of Engineering and Technology (IET) and an Executive Member (Board of Governor) of the China National Committee of International Geosphere–Biosphere Programme and the China Society of Image and Graphics. His research teams won the top three prizes of the IEEE GRSS 2014 Data Fusion Contest, and his students have been selected as the winners or finalists of the IEEE International Geoscience and Remote Sensing Symposium (IGARSS) student paper contest in recent years. He was the General Chair of the 4th IEEE GRSS Workshop on Hyperspectral Image and Signal Processing: Evolution in Remote Sensing (WHISPERS) and a Guest Editor of the IEEE JOURNAL OF SELECTED TOPICS IN APPLIED EARTH OBSERVATIONS AND REMOTE SENSING (JSTARS). He regularly serves as a co-chair of the series SPIE conferences on multispectral image processing and pattern recognition, conference on Asia remote sensing, and many other conferences. He edits several conference proceedings, issues, and geoinformatics symposiums. He also serves as an Associate Editor for the *International Journal of Image and Graphics*, *International Journal of Digital Multimedia Broadcasting*, *Journal of Geo-Spatial Information Science*, and *Journal of Remote Sensing*, and a Guest Editor of *Journal of Applied Remote Sensing* and *Journal of Sensors*. He is currently serving as an Associate Editor for the IEEE TRANSACTIONS ON GEOSCIENCE AND REMOTE SENSING.